A full-Maxwell approach for large angle polar wander of viscoelastic bodies

Hu, Haiyang; van der Wal, Wouter; Vermeersen, Bert

DOI
10.1002/2017JE005365

Publication date
2017

Document Version
Final published version

Published in
Journal of Geophysical Research

AGU PUBLICATIONS

JGR

Journal of Geophysical Research: Planets

RESEARCH ARTICLE
10.1002/2017JE005365

A Full-Maxwell Approach for Large-Angle Polar Wander of Viscoelastic Bodies

H. Hu[1], W. van der Wal[1], and L. L. A. Vermeersen[1]

[1] Department of Aerospace Engineering, Delft University of Technology, Delft, Netherlands

Key Points:
- A semianalytical method for large-angle true polar wander that can deal with a complete scheme of multilayer Maxwell rheology is presented
- We find that using the quasi-fluid approximation leads to a large error for TPW on the Earth, Mars, and Venus
- We show the effect of the permanent shape of an elastic lithosphere and a model that is not in hydrostatic equilibrium on TPW

Correspondence to:
H. Hu,
h.hu-1@tudelft.nl

Citation:
Hu, H., van der Wal, W., & Vermeersen, L. L. (2017). A full-Maxwell approach for large-angle polar wander of viscoelastic bodies. *Journal of Geophysical Research: Planets*, *122*, 2745–2764. https://doi.org/10.1002/2017JE005365

Received 9 JUN 2017
Accepted 10 NOV 2017
Accepted article online 22 NOV 2017
Published online 18 DEC 2017

Abstract For large-angle long-term true polar wander (TPW) there are currently two types of nonlinear methods which give approximated solutions: those assuming that the rotational axis coincides with the axis of maximum moment of inertia (MoI), which simplifies the Liouville equation, and those based on the quasi-fluid approximation, which approximates the Love number. Recent studies show that both can have a significant bias for certain models. Therefore, we still lack an (semi)analytical method which can give exact solutions for large-angle TPW for a model based on Maxwell rheology. This paper provides a method which analytically solves the MoI equation and adopts an extended iterative procedure introduced in Hu et al. (2017) to obtain a time-dependent solution. The new method can be used to simulate the effect of a remnant bulge or models in different hydrostatic states. We show the effect of the viscosity of the lithosphere on long-term, large-angle TPW. We also simulate models without hydrostatic equilibrium and show that the choice of the initial stress-free shape for the elastic (or highly viscous) lithosphere of a given model is as important as its thickness for obtaining a correct TPW behavior. The initial shape of the lithosphere can be an alternative explanation to mantle convection for the difference between the observed and model predicted flattening. Finally, it is concluded that based on the quasi-fluid approximation, TPW speed on Earth and Mars is underestimated, while the speed of the rotational axis approaching the end position on Venus is overestimated.

Plain Language Summary The North and South Poles of the Earth are slowly moving. This is because a large mass can form on the Earth's surface on geologic time scales, which changes how the Earth rotates. Examples of large masses are ice sheets and large mountains. This phenomenon of moving poles takes place on many planets or moons and is referred to as polar wander. Polar wander can be the explanation for why we find surface features at certain locations. For instance, we often observe mountains near the equator of a planet or moon. This is usually the consequence of polar wander: these mountains could have formed anywhere on the planetary body, but due to the polar wander, they eventually end up on the equator. This is the case for the Tharsis plateau on Mars. The mathematical description of polar wander on planetary bodies is difficult, and only approximated solutions have been obtained in the past. Our study establishes a new method which can give an accurate prediction of how the polar wander proceeds through time. We show that previous studies have incorrectly estimated the speed of polar wander on Mars and Venus. With the new method, polar wander on a wide range of planetary bodies can be simulated. Predictions of our method can be compared to observations of surface features to get a better understanding of the interior structure of planets and moons.

1. Introduction

Concerning the study of large-angle true polar wander (TPW) on a viscoelastic body such as terrestrial planets like the Earth, Mars, and Venus, there are currently two types of nonlinear approaches to obtain a time-dependent solution. One of them is from Nakada (2007) which applies an iterative scheme but simplifies the Liouville equation by ignoring the time derivative of the MoI term. This approximation is equivalent to assuming that the rotation axis coincides with the axis of the maximum moment of inertia during the process of TPW. The validity of this assumption was discussed in detail in Cambiotti et al. (2011) who showed that even for the Earth this assumption is not always appropriate. Another approach which is more commonly applied in recent studies was formulated originally by Sabadini and Peltier (1981) and further developed by Sabadini et al. (1982), Spada et al. (1992), and Ricard et al. (1993) which is based on the quasi-fluid approximation.

Mathematically, this approximation is the first-order Taylor expansion of the Love number in the Laplace domain. The consequence of adopting the quasi-fluid approximation is that the elastic response of a Maxwell model is missing, and it also simplifies the individual viscous relaxation of different modes. Hu et al. (2017) tested the validity of the quasi-fluid approximation and showed that it can lead to a large error in the transient behavior of TPW for a model whose strong modes have very different relaxation times. This could lead to erroneous conclusions when the model-predicted TPW speed is compared with the speed that is observed or inferred from surface features (e.g., on Mars, Bouley et al., 2016). The method developed by Hu et al. (2017) is a numerical approach which requires that the change in the inertia tensor is calculated either by convolution or by a finite-element package. Both the numerical convolution and the finite-element package are not suitable for studies of models containing layers with very different viscosities since the large contrast in viscosity results in a large increase in computational time for numerical methods. The increase in the computational time is caused by the fact that the total integration time has to be long to account for the long relaxation time while the integration step size must be small to accurately simulate the layers with short relaxation time.

Another issue which is intensively studied in recent years is the effect of an elastic or highly viscous layer on TPW (Cambiotti et al., 2010; Chan et al., 2014; Harada, 2012; Harada & Xiao, 2015; Mitrovica et al., 2005; Moore et al., 2017; Willemann, 1984). The existence of such a layer can create a delayed readjustment of the equatorial bulge (often called remnant bulge) which significantly changes the behavior of TPW as discussed by Willemann (1984) and Mitrovica et al. (2005). Mitrovica et al. (2005) show the importance of a correct choice for the initial hydrostatic state when the TPW is estimated. They used the fluid tidal Love number which corresponds to the observed flattening instead of the model predicted flattening. Recent studies often assume that this extra flattening comes from mantle convection (Cambiotti et al., 2010; Mitrovica et al., 2005). Alternatively, if we do not assume that the model is in hydrostatic equilibrium, this difference can also come from the elastic lithosphere which has its background shape corresponding to a faster rotational speed. As far as we know, this issue has not been discussed yet. Recent studies concerning the time-dependent solution of long-term large-angle TPW with an elastic or highly viscous lithosphere (Chan et al., 2014; Harada, 2012; Moore et al., 2017) are all based on the method developed by Ricard et al. (1993) and adopt the quasi-fluid approximation.

Compared with the linear approach (e.g., Wu & Peltier, 1984), which can only simulate TPW for small-angle changes, the method from Ricard et al. (1993) enables the study of issues such as the coupling of the rotational perturbation in the X and Y directions. This means that in the body-fixed frame, a mass distribution imbalance in the X-Z plane would cause a rotational perturbation not only in the X-Z plane but also in the Y-Z plane. This coupling effect increases as the rotational speed of the object decreases and can turn TPW into a mega-wobble for some objects like Venus which rotates very slowly (Spada et al., 1996). The phenomenon of the mega-wobble is caused by the increase of the contribution from the mass anomaly itself compared to that of the equatorial bulge readjustment. When the contribution from the equatorial bulge readjustment is dominant, the periodic behavior, often called Chandler wobble, damps out quickly and its secular effect on the long-term TPW can be ignored. However, when the rotational speed decreases which causes the equatorial bulge to decrease, the change in the inertia tensor becomes dominated by the mass anomaly itself. As a result, the rotational behavior resembles the free nutation of a rigid body (Lambeck, 2005). This coupling effect, or periodic behavior, is almost always neglected in the linear scheme for the study of the Earth (e.g., Cambiotti et al., 2010; Wu & Peltier, 1984).

To conclude, a semianalytical approach which can accurately calculate TPW of a Maxwell model in different hydrostatic states is missing. It is the main purpose of this paper to develop such a method and show how more accurate solutions are obtained. We also show if the difference in results between the methods has a significant impact on planetary studies (e.g., observation and modeling) in the following cases: TPW for slowly rotating objects: mega-wobble of Venus; effect of a remnant bulge caused by an elastic or highly viscous lithosphere on large-angle TPW; and TPW on a body that is not in hydrostatic equilibrium.

In section 2, the influence of the quasi-fluid approximation is discussed in more detail and our new method will be presented. Sections 3–5 will cover the above listed issues. Sections 3 and 4 contain a case study of Venus and Mars, respectively, which compares the results obtained in previous studies and that from our new method.

2. Method

The governing equation for the rotation of a rigid body in the body-fixed rotating reference frame is the well-known Euler's equation. As the body becomes deformable, it is often referred to as the Liouville equation. For a torque-free case, it reads (Sabadini et al., 2016)

$$\frac{\mathrm{d}}{\mathrm{d}t}(\mathbf{I}\cdot\boldsymbol{\omega})+\boldsymbol{\omega}\times\mathbf{I}\cdot\boldsymbol{\omega}=0 \tag{1}$$

where $\mathbf{I}$ is the inertia tensor and $\boldsymbol{\omega}$ is the rotational vector whose magnitude is the rotating speed. Both values are defined in a body-fixed coordinate system. When the moment of inertia of the body is perturbed by a geophysical process which causes mass redistribution, the rotational axis shifts, and consequently, the equatorial bulge readjusts. Analytically, given a rotational vector as $\boldsymbol{\omega}=\left(\omega_1,\omega_2,\omega_3\right)^T=\Omega\left(\bar{\omega}_1,\bar{\omega}_2,\bar{\omega}_3\right)^T$, where Ω is the angular speed of the rotation and $\left(\bar{\omega}_1,\bar{\omega}_2,\bar{\omega}_3\right)^T$ is a unit vector which represents the direction of the rotation, the total moment of inertia attributable to such a process is given by (Ricard et al., 1993)

$$\begin{aligned} I_{i,j}(t)=I\delta_{ij}+\frac{k^T(t)a^5}{3G}*\left[\omega_i(t)\omega_j(t)-\frac{1}{3}\Omega(t)^2\delta_{ij}\right] \\ +\left[\delta(t)+k^L(t)\right]*C_{i,j}(t) \end{aligned} \tag{2}$$

where I is the principle moment of inertia of the spherical body in hydrostatic equilibrium, G is the gravitational constant, and a is the radius of the planet. $k^T(t)$ and $k^L(t)$ are the degree 2 potential tidal Love number and load Love number, respectively. Love numbers are obtained by the normal mode method and based on the Maxwell rheology (Farrell, 1972). The asterisk denotes convolution in the time domain. $C_{i,j}$ represents the change in the moments and products of inertia without considering the deformation and this is the triggering load for the TPW. The most difficult part of solving equations (1) and (2) is the convolution of the tidal Love number and the centrifugal potential, in particular, the part $k^T(t)*\omega_i(t)\omega_j(t)$. In the following subsection, we first show how this problem is tackled by adopting the quasi-fluid approximation and the influence of this approximation on calculation of the inertia tensor. Following this subsection a new approach is presented to calculate the MoI equation analytically. Section 2.3 demonstrates how to use the developed algorithm and provides initial results from our method.

2.1. Conventional Approach Based on the Quasi-Fluid Approximation

The tidal Love number in the Laplace domain for a given harmonic degree is expressed as (Peltier, 1974)

$$k^T(s)=k_e^T+\sum_{i=1}^{m}\frac{k_i^T}{s-s_i} \tag{3}$$

where k_e^T is the elastic Love number, k_i^T are the residues of each mode, and s_i are the inverse relaxation times. This form of the Love number contains all the information about how a multilayered Maxwell body deforms: an instantaneous elastic response characterized by k_e^T followed by viscous relaxation of separate modes characterized by their different inverse relaxation time s_i and mode strength $-k_i/s_i$. We call this form of the Love number the full-Maxwell rheology scheme, as opposed to the quasi-fluid approximation introduced below.

In order to solve equation (2), Ricard et al. (1993) took the quasi-fluid approximation which approximates the tidal Love number with its first-order Taylor expansion:

$$\begin{aligned} k^T(s)&\approx k_e^T-\sum_{i=1}^{m}\left(\frac{k_i^T}{s_i}+\frac{k_i^T s}{s_i^2}\right) \\ &=k_f^T(1-T_1 s) \end{aligned} \tag{4}$$

where k_f^T is the fluid Love number which is the sum of the mode strength:

$$k_f^T=k_e-\sum_{i=1}^{m}\frac{k_i^T}{s_i} \tag{5}$$

The time constant T_1 is

$$T_1=\frac{1}{k_f^T}\sum_{i=1}^{m}\frac{k_i^T}{s_i^2} \tag{6}$$

Thus, by taking the quasi-fluid approximation, all information for a viscoelastic layered model is combined into one constant T_1. Because of the k_i/s_i^2 term, this constant is dominated by the slowest modes. Thus, applying

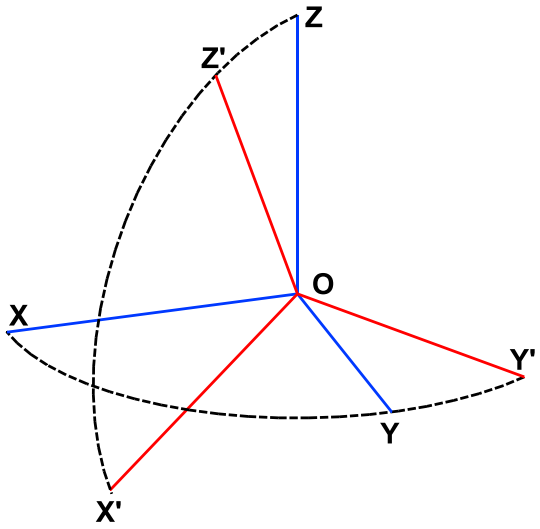

Figure 1. O-*X*<mathdollar>YZ is the body-fixed frame where the *Z* axis is the original rotational axis. O-*X*′*Y*′*Z*′ is the bulge-fixed frame where the *Z*′ axis is the instantaneous rotational axis and the *X*′ axis lies within the *Z*-*Z*′ plane.

the quasi-fluid approximation on a physical model which contains modes with both very long and short relaxation times will result in a large bias. It can also be seen that with this approximation, the elastic response as well as the viscous relaxation characterized by the function $1/(s - s_i)$ in the Laplace domain ($e^{s_i t}$ in the time domain) are missing (as will be shown in equation (7)); therefore, the ongoing deformation does not agree with the complete Maxwell rheology scheme. The convolution of equation (4) with a linear load function $F(t) = a + bt$, where a, b are constants, results in a time domain response of the form

$$R(t) = k_f^T F(t) - F'(t) k_f^T T_1 \tag{7}$$

where the derivative $F'(t) = b$ and $R(t)$ is the response function. This response demonstrates the effect of the quasi-fluid approximation: for a near-constant load ($F'(t) \approx 0$), the response reaches its fluid limit $k_f^T F(t)$ immediately without the time-dependent viscous behavior. This means that when the speed of TPW is very slow compared to the characteristic relaxation speed of the body, the results based on the quasi-fluid approximation approach those which are obtained from the fluid limit method which diagonalizes equation (2), such as in Matsuyama and Nimmo (2007). For other loads which change linearly in time, the instantaneous fluid limit response $k_f^T F(t)$ is shifted by a value which is proportional to the speed of the change of the load, as given by the second term of the equation (7). For the complete Maxwell rheology scheme, the original form of the Love number (equation (3) needs to be convoluted with the loading function, resulting in damping of this part with a function of e^{-At}, where A is a positive constant. As a result, compared to the original Maxwell rheology, the response of a Heaviside or fast changing load based on the quasi-fluid approximation will likely result in a very different TPW path. For example, the change in the inertia tensor due to an impact crater which appears instantly and is preserved afterward is a Heaviside load to the planet.

Next, we quantitatively show that adopting quasi-fluid approximation can either underestimate or overestimate the equatorial readjustment for certain components of the inertia tensor in the normal polar wander case and in the mega-wobble case. Substituting equation (4) into (2) gives the change in the moment of inertia as (Ricard et al., 1993)

$$\begin{aligned}\Delta I_{i,j}(t) = {} & \frac{k_f^T a^5}{3G}\left[\omega_i(t)\omega_j(t) - \frac{1}{3}\Omega(t)^2\delta_{ij}\right] \\ & - \frac{k_f^T a^5}{3G} T_1 \left[\dot{\omega}_i(t)\omega_j(t) + \omega_i(t)\dot{\omega}_j(t) - \frac{2}{3}\omega_l(t)\omega_l(t)\delta_{ij}\right] + E_{ij}\end{aligned} \tag{8}$$

where $E_{i,j}(t)$ and $\dot{E}_{i,j}(t)$ are obtained by convolving $C_{i,j}(t)$ and $\dot{C}_{i,j}(t)$ with $\delta_{i,j} + k^L(t)$. We compare the change in the moment of inertia calculated by equations (8) and (2) to show the influence of adopting the quasi-fluid approximation. The latter is obtained by numerical calculation of the convolution. As a representative of terrestrial planets, we use a SG6 Earth model (which represents a multilayered model with interior density, rigidity, and viscosity change) and let the rotational axis move in two ways:

1. The rotational axis drifts with a constant speed along the *X*-*Z* plane in the body-fixed coordinates for 90°. This is to simulate the normal polar wander case for fast-rotating planets such as the Earth and Mars.
2. The rotational axis initially stays at 30° colatitude and 0° longitude in the *X*-*Z* plane and moves longitudinally with a constant speed along the 30° colatitude circle for 720°. This is to simulate the mega wobble for very slowly rotating objects such as Venus.

In the first case, the drift speed of the rotational axis is chosen to be fast enough to view the effect of the quasi-fluid approximation. We define a bulge-fixed frame whose *Z*′ axis coincides with the instantaneous rotational axis and whose *X*′ axis lies within the *Z*-*Z*′ plane as shown in Figure 1. So a pure rotation (around *Y*′ axis) can transform the body-fixed frame into the bulge-fixed frame.

Figure 2 gives the change in the six components of the MoI tensor in the bulge-fixed frame. In this figure, the differences in the I_{11}, I_{22}, andI_{33} are small, but the most important component I_{13} calculated with the quasi-fluid approximation is significantly larger than the accurate value. The magnitude of the I_{13} in the bulge-fixed

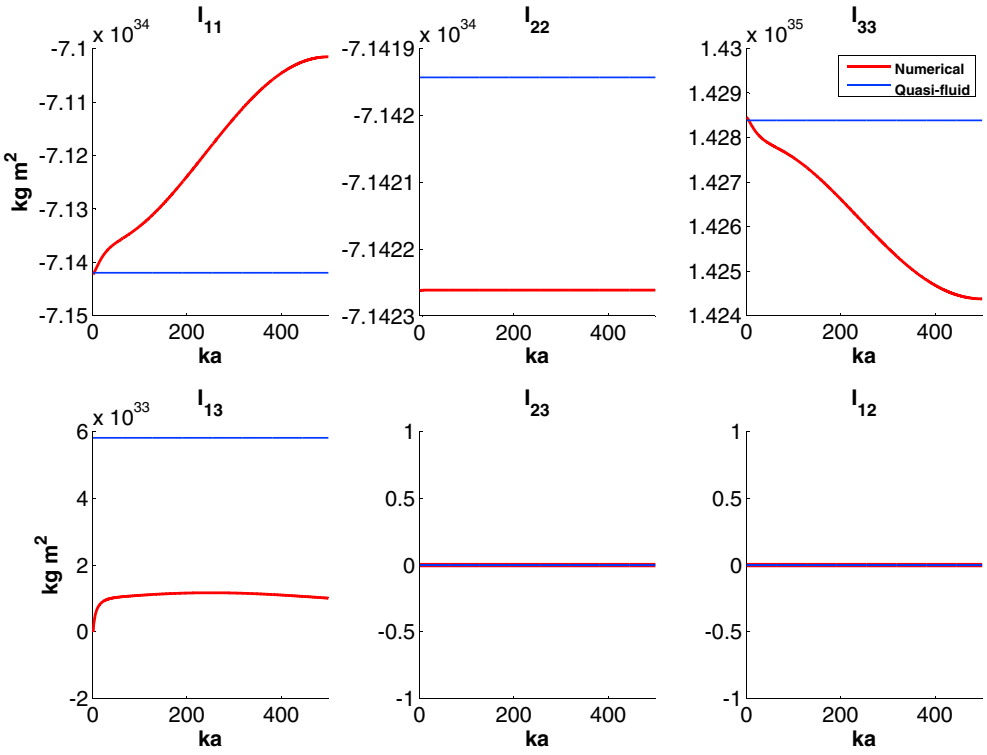

Figure 2. Normal polar wander case: change in the six components of the MoI tensor when the rotational axis initially stays at 30° colatitude and 0° longitude in the *X-Z* plane and precesses with a constant speed along the 30° colatitude circle for 720° in 500 ka. Red lines are the accurate results and blue lines are from the quasi-fluid approximation.

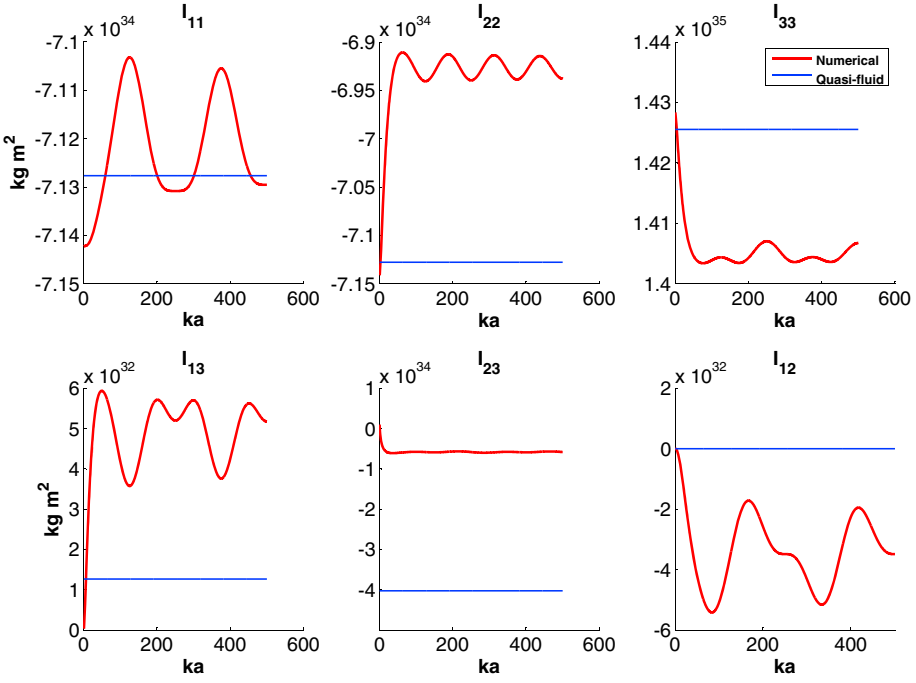

Figure 3. Mega-wobble case: change in the six components of the MoI tensor. The rotational axis initially stays at 30° colatitude and 0° longitude in the *X-Z* plane and precesses longitudinally with a constant speed along the 30° colatitude circle for 720° in 600 ka. Red lines are the accurate results, and blue lines are from the quasi-fluid approximation.

frame determines how fast the equatorial bulge readjusts. A larger value of I_{13} suggests a slower readjustment (if the readjustment is complete, then the rotational axis coincides with the new principle axis and I_{13} would be zero). So adopting the quasi-fluid approximation in the normal polar case causes a large underestimation for the speed of the equatorial bulge readjustment.

For the second case where the rotational axis tends to wobble around a fixed point, in the bulge-fixed frame, the I_{23} implies the readjustment in the direction along the track of the rotational axis (called along-track direction in the following) and I_{13} gives the readjustment in the direction which is perpendicular to the plane that contains the along-track direction and the rotational axis (called normal direction in the following). The results are shown in Figure 3. For components I_{11}, I_{22}, and I_{33}, the quasi-fluid approximation misses the small oscillations but the differences are still very small between the two methods; thus, for these three components the error introduced by the approximation can be ignored. However, the magnitude of the along-track component I_{23}, is largely underestimated just like the I_{13} component in Figure 2 (I_{13} is the along-track component for the normal polar wander case). On the other hand, the normal directional component I_{13} in Figure 3 is underestimated by the quasi-fluid approximation which suggests an overestimation of the equatorial bulge readjustment in this direction.

The key information obtained in this subsection is that by adopting the quasi-fluid approximation, the speed for equatorial readjustment can be, depending on the model and load, largely underestimated in the along-track direction but overestimated for the mega wobble case in the normal direction. These are the main reasons for the difference of the TPW path calculated by different methods which will be discussed in sections 3 and 4.

2.2. A New Approach

In order to eliminate the convolution in the part $k^T(t) * \omega_i(t)\omega_j(t)$ while staying consistent with the fundamental rheology of the system, we adopt the strategy of approximating the load term $\omega_i(t)\omega_j(t)$ instead. Within the considered time period T_n, at time $t = T_p$, $p = 0, 1, \ldots, n$, values of $\omega_i(t)$, $i = 1, 2, 3$ are known, then we have $\omega_i(T_p) = W_{i,p}$. Assuming that $\omega_i(t)$, $i = 1, 2, 3$ changes linearly between each time step, $\omega_i(t)$ can be written as a piecewise linear function:

$$\omega_i(t) = \sum_{p=1}^{n} \omega_{i,p} \tag{9}$$

where

$$\omega_{i,p} = \left(W_{i,p-1} + \frac{W_{i,p} - W_{i,p-1}}{T_p - T_{p-1}} \left(t - T_{p-1}\right) \right) H\left(t - T_{p-1}\right) H\left(T_p - t\right) \tag{10}$$

and $H(t)$ is the Heaviside step function. With this form, $k(t) * \omega_i(t)\omega_j(t)$ and its derivative can be expressed analytically by applying the Laplace transformation

$$k^T(t) * \omega_i(t)\omega_j(t) = \mathcal{L}^{-1}[\mathcal{L}[k^T(t) * \omega_i(t)\omega_j(t)]] \tag{11}$$

where $\mathcal{L}$ and $\mathcal{L}^{-1}$ stand for the Laplace and inverse Laplace transformation, respectively. The explicit expression of equation (11) can be found in Appendix A as equations (A1a)–(A1c). Substituting equations (A1a)–(A1c) into (2), the inertia tensor and its derivative at time $t = T_n$ can be expressed analytically as

$$I_{i,j}(T_n) = I\delta_{i,j} + \frac{a^5}{3G}\left[(A_{i,j}(T_n) + B_{i,j}) - \frac{1}{3}\sum_{k=1}^{3}(A_{k,k}(T_n) + B_{k,k}) \right] + E_{i,j}(T_n) \tag{12a}$$

$$\dot{I}_{i,j}(T_n) = \frac{a^5}{3G}\left[(C_{i,j}(T_n) + D_{i,j}) - \frac{1}{3}\sum_{k=1}^{3}(C_{k,k}(T_n) + D_{k,k}) \right] + \dot{E}_{i,j}(T_n) \tag{12b}$$

where expressions for $A_{i,j}(t)$, $B_{i,j}(t)$, $C_{i,j}(t)$ and $D_{i,j}(t)$ can be found in Appendix A. When $t = T_p$ with $p = 0, 1, \ldots n$ and $\omega_i(T_p) = W_{i,p}$ with $p = 0, 1, 2 \ldots n-1$ are given, equations (12a) and (12b) express the moments and products of inertia and its derivative as a function of $W_{i,n}$. Then $W_{i,n}$ can be solved by equation (1). To this end, it helps to see the problem as a global optimization problem: we seek the value of $W_{i,n}$ in the neighborhood of $W_{i,n-1}$ so that the value of $|\frac{\mathrm{d}}{\mathrm{dt}}(\mathbf{I}\cdot\boldsymbol{\omega}) + \boldsymbol{\omega}\times\mathbf{I}\cdot\boldsymbol{\omega}|$ is minimized. As a result, the method which is introduced in Hu et al. (2017) as *algorithm 2* (p. 10) can be applied. This method applies the linearized form of the Liouville equation and an iteration procedure to obtain $W_{i,n}$. It will be briefly explained in the following and outlined in Appendix B.

This algorithm is validated in (Hu et al., 2017) by both the linear (Wu & Peltier, 1984) and the nonlinear method (Ricard et al., 1993) as shown in Figure D1 in Appendix D. We define the perturbed rotational vector as

$$\boldsymbol{\omega}' = \Omega(m_1, m_2, 1 + m_3)^T \tag{13}$$

where m_1, m_2, and m_3 are small real numbers. The Liouville equation can be linearized to obtain the form (Hu et al., 2017)

$$m_1(t) = \frac{\Delta I_{13}(t)}{C - A} + \frac{C\Delta \dot{I}_{23}(t)}{\Omega(C - A)(C - B)} \tag{14a}$$

$$m_2(t) = \frac{\Delta I_{23}(t)}{C - B} - \frac{C\Delta \dot{I}_{13}(t)}{\Omega(C - A)(C - B)} \tag{14b}$$

$$m_3(t) = -\frac{\Delta I_{33}}{C} \tag{14c}$$

In equations (14a)–(14c), the terms of the inertia tensor, A, B, C and $I_{13}, I_{23}, \dot{I}_{13}, \dot{I}_{23}$ are not in the body-fixed frame but in the bulge-fixed frame. The transformation matrix from the body-fixed frame to the bulge-fixed frame by a pure rotation can be obtained as

$$\mathbf{Q} = \begin{pmatrix} \omega_3 + \frac{\omega_2^2}{1+\omega_3} & -\frac{\omega_1\omega_2}{1+\omega_3} & \omega_1 \\ -\frac{\omega_1\omega_2}{1+\omega_3} & 1 - \frac{\omega_2^2}{1+\omega_3} & \omega_2 \\ -\omega_1 & -\omega_2\omega_3 & \end{pmatrix} \tag{15}$$

A coordinate transformation is required before we can substitute the value of the inertia tensor calculated from equations (12a) and (12b). The detailed procedure of algorithm 2 in Hu et al. (2017) is given in Appendix B.

In general, the only assumptions we make in the entire calculation in this study are two linear approximations: the changes in the rotational vector and the inertia tensor (see equation (10) in Hu et al. (2017)) are small in each step and can be treated as linear. These assumptions are valid when the step sizes ($\Delta t_p = T_p - T_{p-1}, p = 2, 3, \ldots, n$) are small enough. Since we do not approximate Love numbers, our method gives the TPW path for a viscoelastic body which is consistent with the complete scheme of Maxwell rheology. We will label our method in the following as full-Maxwell method.

2.3. Initial Setting and Validation

One of the major factors that controls the TPW behavior is the shape of the equatorial bulge (and the tidal bulge which is discussed in Hu et al., 2017). When the interior model and rotational speed is given, this shape is controlled by the hydrostatic state of the model. Due to the limitation of the method, previous studies based on either linear (Sabadini et al., 1982; Wu & Peltier, 1984) or nonlinear (Chan et al., 2014; Moore et al., 2017; Ricard et al., 1993) approaches can only simulate TPW on a model which is assumed to be in hydrostatic equilibrium. However, as will be shown in section 5, the choice of the hydrostatic state can have a significant impact on the TPW behavior. With our method, we can choose the hydrostatic state of the model at which the TPW starts.

To simulate the TPW of a body at a certain hydrostatic state, we need to apply a centrifugal force to the model for a certain length of time. If the rotational vector at the start of the simulation is given by $\boldsymbol{\omega}_0 = \Omega(0, 0, 1)^T$, applying centrifugal force to the model for a duration of T_h is expressed in our scheme as

$$T_0 = 0 \tag{16a}$$

$$T_1 = T_h \tag{16b}$$

$$\left(W_{1,0}, W_{2,0}, W_{3,0}\right)^T = \left(W_{1,1}, W_{2,1}, W_{3,1}\right)^T = \boldsymbol{\omega}_0 \tag{16c}$$

The triggering load $E_{i,j}(t)$ needs to be applied at $t = T_h$ to start the TPW. To simulate a model in hydrostatic equilibrium, T_h needs to be large enough so that all modes of the model are sufficiently relaxed. In order to achieve this, we can choose a T_h so that the slowest mode is relaxed more than 99.999%. Assuming s_1 is the slowest mode,

$$1 - e^{s_1 T_h} > 0.99999 \tag{17}$$

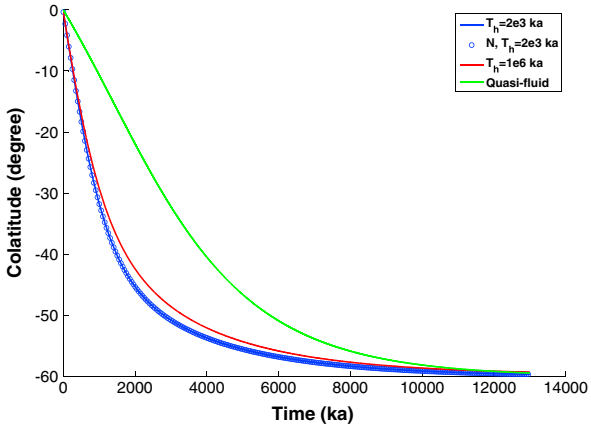

Figure 4. Polar wander in the *X*-*Z* plane for the SG6 Earth model triggered by a point mass of 2×10^{19} kg attached at the surface at 30° colatitude.

translates into

$$T_h > \frac{-11.513}{s_1} \tag{18}$$

This choice is similar to that in Hu et al. (2017), which sets T_h so that $k^T(T_h) > 99.95\%\, k_f^T$, but much more strict. If the model contains a very slow and strong mode, we can obtain a very large value of T_h and this will cause an extremely long calculation time for a pure numerical method (Hu et al., 2017). By expressing the inertia tensor analytically, a very large T_h can be dealt with. Eventually, there is no limit for the choice of T_h as well as the initial loading $\boldsymbol{\omega}_0$ as long as numerical errors (e.g., truncation error) are avoided. As a result, TPW for a body in a different hydrostatic state can be obtained. This makes our method suitable to study the effect of a remnant bulge or TPW on a model without hydrostatic equilibrium as will be shown and discussed in detail in sections 4 and 5.

The algorithm, as shown in Appendix B, was developed in Hu et al. (2017). The main idea is to decouple the two governing equations. The MoI equation was solved by either direct convolution or from a finite element method and the result is fed back into the linearized Liouville equation and solved by an iterative procedure. Such algorithm has been validated by both comparing to the linear (Wu & Peltier, 1984) and nonlinear method (Ricard et al., 1993) in Figures 6 and 9 of Hu et al. (2017). The difference between the method in this paper and that of Hu et al. (2017) is that here the MoI equation is solved analytically with the assumption that the rotational vector changes linearly during each time step of TPW. If the step size is set to be much smaller than the relaxation time of the dominant modes, which is the same requirement for calculating TPW, the analytical solution of the MoI equation with the linear assumption will be sufficiently equivalent to the result from direct convolution. Therefore, the TPW solution generated in this paper can approach that from Hu et al. (2017) for a small enough step size. We first demonstrate the result of TPW calculated with $T_h = 2,000$ ka, which is the choice in Hu et al. (2017) for a six-layer incompressible Earth model SG6 (Table 2 in the same paper), and a much higher value ($T_h = 10^6$ ka) for which the model can be considered in hydrostatic equilibrium (equation (18) holds). We place a stationary ($k^L(t) = 0$) mass anomaly, which means that the mass anomaly does not "sink" into the body, at the surface at 30° colatitude. Here we do not consider the effect of the remnant bulge (which will be discussed in detail in section 4), so we ignore the slowest mode generated by the lithosphere (its viscosity is set to 10^{31} Pa s to calculate the Love numbers). We also include the result obtained by the quasi-fluid approximation according to Ricard et al. (1993).

As can be seen in Figure 4, the result obtained for $T_h = 2,000$ ka by the full-Maxwell method is very close (within 0.05% difference) to the result of the numerical method from Hu et al. (2017), for a step size of 5 ka. It is also clear that choosing $T_h = 2,000$ ka still shows a TPW path that is different from that of a body which can be considered to be in hydrostatic equilibrium ($T_h = 10^6$ ka). This suggests the sensitivity of the TPW to a small deviation from its hydrostatic equilibrium. So choosing T_h large enough is the first guarantee that the correct TPW path for models with hydrostatic equilibrium is obtained.

The computational cost of our method depends on three factors: (1) the complexity of the layered model, or more precisely, the number of the modes in the Love numbers; (2) the number of iteration necessary to obtain a convergent result in each step; and (3) the number of time steps. The computational time increases roughly linearly with these factors. For the results shown in Figure 3, which is for a SG6 Earth model that contains 12 modes, the number of time steps is 2,600 (each step is 5 ka) and every step requires 50 (first step) to 18 (last step) iterations. The program is written in *MATLAB* and the total computational time on our desktop computer is about 3 min. Compared with the numerical computation (Hu et al., 2017) which is about several hours, the speed from the semianalytical approach is much faster.

Based on the analysis in section 2.1, the largely underestimated TPW speed by adopting the quasi-fluid approximation is caused by the underestimation of the speed of the equatorial readjustment for the case of Earth and Mars. For the mega-wobble case in Venus, the situation can be quite different as will be discussed in the following section.

3. Mega-Wobble: TPW on Venus

The linearized Liouville equation (equations (14a)–(14c)) is obtained by two fundamental assumptions. First, during the TPW, the components of the inertia tensor satisfy $I_{33}(C) > I_{11}(A)$ and $I_{33}(C) > I_{22}(B)$. Second, the periodic terms which represent the Chandler wobble can be ignored. While these assumptions are true for cases like Mars and the Earth, it can be invalid for some slowly rotating objects such as Venus. Since the rotational speed of Venus is so slow that its equatorial bulge is also extremely small, the difference of the two principle moment of inertia: $C - A$, which can be calculated by

$$C - A = \frac{k_f^T a^5 \Omega^2}{3G} \tag{19}$$

for Venus is less than 1.5×10^{-5} of that for Earth. For magnitudes of a mass anomaly of 10^{-5} or 10^{-6} of the total mass of the planet considered in Spada et al. (1996), depending on the depth and position, the moment around the rotational axis may not be the largest of the diagonal components anymore ($C > A, B$ are not satisfied). Furthermore, the period of the wobble, which can be estimated as $\frac{2\pi}{\Omega}\sqrt{\frac{AB}{(C-A)(C-B)}}$ (see equation (26)) when $C > A, B$, is about 4 months (depending on the interior model) on Earth or Mars but can be, depending on the interior model, over 10 Ma on Venus. Because of such low frequency, the periodic terms will have a secular effect for TPW on Venus and cannot be ignored as for the Earth and Mars. Therefore, in order to study TPW on Venus, it is necessary to first derive a new set of linearized Liouville equations suitable for a body with a very long wobble period. The linearized Liouville equation for a triaxial body reads (Sabadini et al., 2016)

$$\dot{m}_1 = -\frac{C-B}{A}\Omega m_2 + \frac{\Omega}{A}\Delta I_{23} - \frac{\Delta \dot{I}_{13}}{A} \tag{20a}$$

$$\dot{m}_2 = \frac{C-A}{B}\Omega m_1 - \frac{\Omega}{B}\Delta I_{13} - \frac{\Delta \dot{I}_{23}}{B} \tag{20b}$$

$$\dot{m}_3 = -\frac{\Delta \dot{I}_{33}}{C} \tag{20c}$$

We first deal with the cases of $C>A$, $C>B$, and $C<A$, $C<B$. By assuming that the change in the moment of inertia is linear, equations (20a)–(20c) can be solved analytically. The result contains the non-periodic terms in equations (14a)–(14c) and periodic terms

$$\begin{aligned}\tilde{m}_1(t) = &\sqrt{\frac{B}{A(C-A)^3(C-B)\Omega^2}}\sin\left(\sqrt{\frac{(C-A)(C-B)}{AB}}\Omega\Delta t\right)\left((A-C)\Delta I_{23}(t) + C\Delta \dot{I}_{13}(t)\right)\\ &-\cos\left(\sqrt{\frac{(C-A)(C-B)}{AB}}\Omega\Delta t\right)\left(\frac{\Delta I_{13}(t)}{C-A} + \frac{C\Delta \dot{I}_{23}(t)}{\Omega(C-A)(C-B)}\right)\end{aligned} \tag{21}$$

$$\begin{aligned}\tilde{m}_2(t) = &\sqrt{\frac{A}{B(C-A)(C-B)^3\Omega^2}}\sin\left(\sqrt{\frac{(C-A)(C-B)}{AB}}\Omega\Delta t\right)\left((C-B)\Delta I_{13}(t) + C\Delta \dot{I}_{23}(t)\right)\\ &-\cos\left(\sqrt{\frac{(C-A)(C-B)}{AB}}\Omega\Delta t\right)\left(\frac{\Delta I_{23}(t)}{C-B} + \frac{C\Delta \dot{I}_{13}(t)}{\Omega(C-A)(C-B)}\right)\end{aligned} \tag{22}$$

When the period of the wobble becomes very long and the step size Δt is small enough, the magnitude of $\sqrt{\frac{(C-A)(C-B)}{AB}}\Omega\Delta t$ in the trigonometric functions is very small, and we can apply $\sin(\theta)\approx\theta$ and $\cos(\theta)\approx 1-\theta^2/2$. Applying these approximations, combining equations (14a)–(14c), (21), and (22) and ignoring the derivative terms of the inertia tensor gives

$$m_1(t) = \frac{(C-B)\Omega^2\Delta I_{13}(t)\Delta t^2 + 2B\Omega\Delta I_{23}(t)\Delta t}{2AB} \tag{23a}$$

$$m_2(t) = \frac{(C-A)\Omega^2\Delta I_{23}(t)\Delta t^2 - 2A\Omega\Delta I_{13}(t)\Delta t}{2AB} \tag{23b}$$

$$m_3(t) = -\frac{\Delta I_{33}}{C} \tag{23c}$$

Table 1
Venus Model

Outer radius (km)	Density (kg m^{-3})	Shear modulus (Pa)	Viscosity (Pa s)
6,052	2,900	0.36×10^{11}	∞
6,002	3,350	0.68×10^{11}	0.6×10^{21}
5,500	3,725	0.93×10^{11}	1.6×10^{21}
5,200	4,900	2.07×10^{11}	6.4×10^{21}
3,250	10,560	0	0

The derivation for other situations such as $B < C < A$or $B > C > A$ are shown in Appendix C. Note that in equations (23a)–(23c), as well as in equations (C5a), (C5b), (C6), and (C6b), we do not have the $C - A$ or $C - B$ terms in the denominator; thus, these expressions have no singularity problem for $C = B$ or $C = A$. When TPW on a very slowly rotating object like Venus is calculated, equations (23a)–(23c) instead of equations (14a)–(14c) should be applied. Basically, equations (14a)–(14c) and equations (23a)–(23c) give two extreme situations for calculating the rotational perturbation. When the step size of the calculation Δt can be set to much larger than the Chandler period, equations (14a)–(14c) should be used to give the secular behavior. When the step size Δt is chosen to be much smaller than the period of the Chandler wobble, equations (23a)–(23c) can give the periodic "short"-term behavior which leads to the mega-wobble on Venus or, when the step size is set to days, the Chandler wobble on Earth or Mars.

Next, we apply our method to a model of Venus and test some results obtained in Spada et al. (1996) who apply the quasi-fluid approximation. We create a five-layer Venus model which approximates the density and rigidity profile used in Armann and Tackley (2012), and the viscosities are chosen similar to those of Earth. The interior properties are shown in Table 1. The effect of a remnant bulge is not included here and will be discussed in the next section.

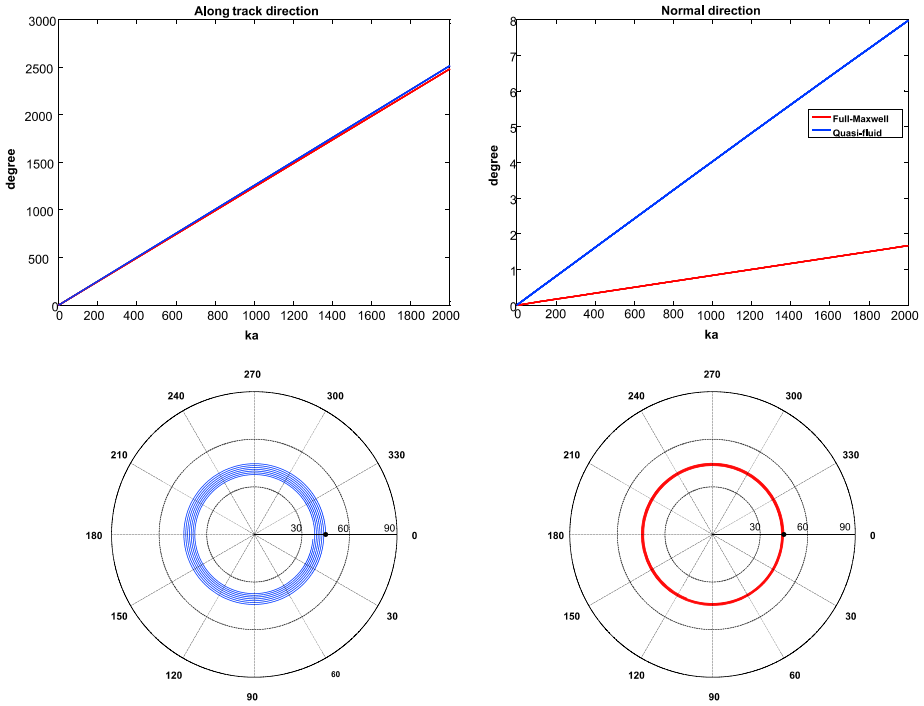

Figure 5. A point mass of -5×10^{18} kg is attached at the surface at 45° colatitude. (top row)The displacement of the rotational axis in the along-track and normal direction. (bottom row) The movement of the mass anomaly in the bulge-fixed frame where the rotational axis is always pointing upward at the center. Blue lines are obtained by applying the quasi-fluid approximation, and red lines are from the full-Maxwell method. The black dots are the original locations of the mass anomalies in the bulge-fixed frame.

For this model, the period $\frac{2\pi}{\Omega}\sqrt{\frac{AB}{(C-A)(C-B)}}$ is about 11.45 Ma. The step size needs to be much smaller than this value; therefore, a value of less than 5,000 years is sufficient to obtain an accurate solution. One way to test if the chosen step size is indeed small enough is to recalculate the TPW with half of the step size. If the chosen step size is indeed sufficiently small, the result will not change significantly. We first simulate the TPW on Venus driven by a negative mass anomaly of magnitude 5×10^{18} kg (which is about the maximum value simulated by Spada et al. (1996)) which is attached at the surface at 45° colatitude. We decompose the displacement of the rotational axis in the direction which lies in the plane that contains the mass anomaly (normal direction) and the along-track direction. The result is shown in Figure 5. As we can see, for the along-track displacement which describes the long-term wobble of the rotational axis around the mass anomaly, the results from the two methods differ less than 1%. However, for the displacement in the normal direction, representing the movement of the rotational axis toward the negative mass anomaly, the result obtained based on the quasi-fluid approximation overestimates the speed. The agreement in the along-track direction displacement and a disagreement in the normal direction displacement between the two methods can be explained by the small contribution of the equatorial bulge readjustment to the rotational perturbation for Venus. As pointed out by Spada et al. (1996), for Venus, the rotational behavior is largely dominated by the long-term wobble which resembles the free nutation of a rigid body. The long-term wobble is mainly caused by the mass anomaly itself, while the equatorial readjustment contributes very little. Based on the discussion of Figure 3, the component I_{23} also contributes to the along-track speed of the wobble. This component is largely overestimated by the quasi-fluid approximation, but since its magnitude is much smaller than the contribution from the mass anomaly itself (less than 1% in this case), the difference between the two methods can be ignored. However, the damping of the oscillatory motion, or the displacement of the rotational axis in the normal direction, is solely controlled by the viscous relaxation of the body, specifically the component I_{13} in Figure 3. Since this component is underestimated by the quasi-fluid approximation, the rotational behavior on Venus obtained by adopting the approximation results in too much damping.

In the study of terrestrial planets whose tidal bulge can be ignored, like Earth, Mars, Venus, and Mercury, we may see certain geographic features (e.g., the supercontinent Pangaea on the Earth or the Tharsis plateau on Mars) which have the potential to cause (or have caused) polar wander. Based on an interior model and TPW history, we can estimate the age of the feature or the history of its relocation by its (estimated) former and current latitude since we know that positive mass anomaly tends to relocate toward equator and negative one toward the pole. The latitudinal information in many situations is much more important than the longitudinal one if the body is not tidally locked. As a result, correctly estimating the TPW speed in the latitudinal (normal) direction is crucial for a better understanding of the planet reorientation. In the following the same Venus model is used and several different magnitudes of mass anomaly are tested. We compare the difference in speed as a function of colatitude of the mass anomaly in the normal direction between the two methods. Magnitudes of mass anomaly 1×10^{16}, 1×10^{17}, 1×10^{18}, and 5×10^{18} kg are chosen, which are about 10^{-5} to 10^{-6} times of the total mass of Venus, similar to the values chosen in Spada et al. (1996). The results are shown in Figure 6. Generally, methods based on the quasi-fluid approximation overestimate the normal-directional speed by a factor of 3 to 5.

Spada et al. (1996) state that for the same mass anomaly, the instantaneous velocity of rotational pole on Venus is about 30 times larger than that of Earth and Mars. But they compared the complete rotational behavior of Venus whose largest part is the wobble with the secular rotational behavior of Earth and Mars in which the Chandler wobble has been filtered out. A more proper comparison would be either between the speed of Chandler wobble on Earth or Mars with the mega-wobble on Venus, or between the secular speed of rotational variation on Earth or Mars and the normal-directional speed of the rotational axis on Venus. In the latter case, for an Earth, Mars, and Venus model with the same average viscosity (ranging from 10^{20} to 10^{22} Pa s), it can be shown that TPW on Earth and Mars is 10 to 15 times larger than the normal-directional speed of Venus' rotational axis for the mass anomalies considered in this study. This means that for the same scale of mass anomaly, it will take much longer on Venus than on Earth or Mars before it can reach the pole or equator. The knowledge of Venusian viscosity is very limited, if the observed normal-directional change of Venus' rotational axis is out of this range (1/10 to 1/15 times of the Earth's TPW), then the average viscosity of Venus must be lower or higher than that of the Earth.

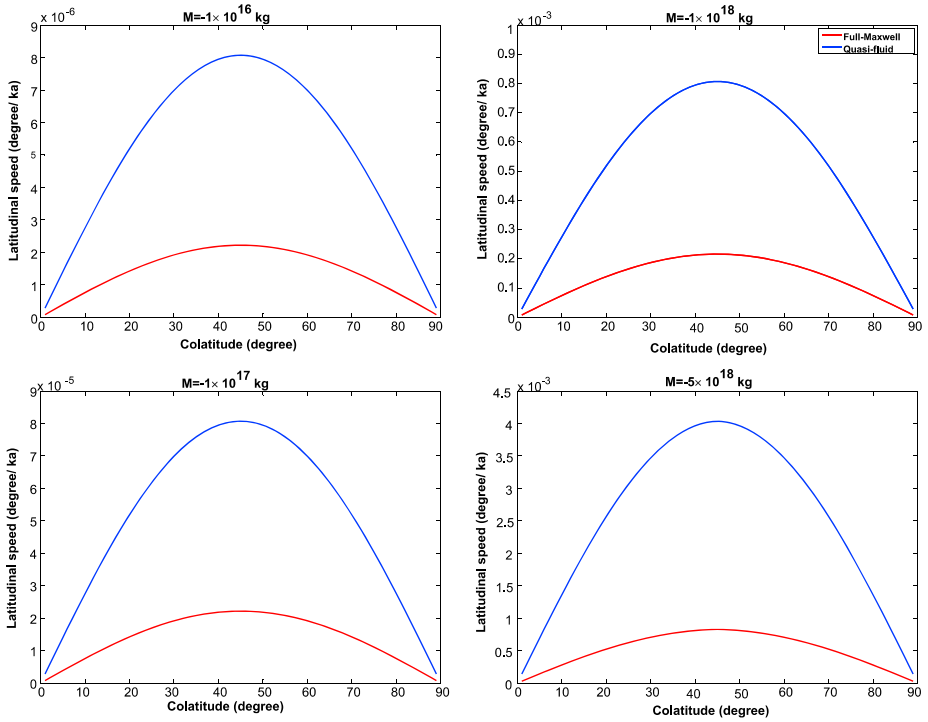

Figure 6. Normal directional speed of the rotational axis toward the mass anomaly as a function of the colatitude.

The results we obtained in this section (e.g., the speed in Figures 5 and 6) are, of course, dependent on the interior model of Venus. With different viscosities (10^{19} Pa s to 10^{22} Pa s), the TPW speed can be very different but adopting the quasi-fluid approximation always largely overestimates the normal-directional speed.

4. Effect of a Remnant Bulge on TPW and a Study of Mars

For a viscoelastic model which can be sufficiently relaxed, a positive mass anomaly with any magnitude will end up at the equator, while a negative mass anomaly will eventually reach the poles. However, most of the observed geophysical features which are thought to have triggered a reorientation, such as the Tharsis plateau on Mars (Bouley et al., 2016) or Sputnik Planitia on Pluto (Keane et al., 2016), are not located exactly at the equator. A common explanation is that certain parts of the planet, usually the lithosphere which is considered to be elastic or to have a very high viscosity, have not yet relaxed, preventing the mass anomaly from being relocated further. The effect of such elastic or highly viscous lithosphere on TPW has been studied for the linear scheme (e.g., Cambiotti et al., 2010; Mitrovica et al., 2005), and the nonlinear scheme with the quasi-fluid approximation (e.g., Chan et al., 2014; Harada, 2012; Moore et al., 2017). Here we demonstrate the effect of a remnant bulge on the large-angle TPW with the full-Maxwell method.

First, the origin of the remnant bulge is shown using the normal mode method. This has also been discussed by Moore et al. (2017). The remnant bulge, either formed by an elastic layer or a highly viscous layer, appears because of a certain mode(s) which has a much longer (or infinite) relaxation time compared to other dominant relaxation modes of the model. We demonstrate this with a simple two-/three-layer Earth models with and without a lithosphere of varying viscosity. In Table 2, the physical properties of the models are shown.

Table 2
Properties of the Two-/Three-Layer Earth Models (M1 – M5)

Layer	Outer radius (km)	Density (kg m^{-3})	Shear modulus (Pa)	Viscosity (Pa s)
Lithosphere	6,371	4,448	1.7×10^{11}	$1 \times 10^{21,24,26,29}, \infty$
Mantle	6,361	4,448	1.7×10^{11}	1×10^{21}
Core	3,480	10,977	0	0

Table 3
Potential Tidal Love Number of Models M1–M5

	M1 (10^{21} Pa s)		M2 (10^{24} Pa s)		M3 (10^{26} Pa s)		M4 (10^{29} Pa s)		M5 (∞ Pa s)	
Modes	s_i	$-k_i/s_i$	s_i	$-k_i/s_i$	s_i	$-k_i/s_i$	s_i	$-k_i/s_i$	s_i	$-k_i/s_i$
k_e		0.3449		0.3449		0.3449		0.3449		0.3449
T_1			−0.5341e−1	0.4731e−2	−0.5343e−3	0.4204e−2	−0.5343e−6	0.4200e−2		
T_2			−0.7886e−1	0.3045e−2	−0.2764e−1	0.2035e−2	−0.2713e−1	0.2027e−2	−0.2712e−1	0.2027e−2
C_0	−0.4086	0.2376	−0.4208	0.2337	−0.4193	0.2351	−0.4193	0.2352	−0.4193	0.2352
M_0	2.225	0.4591	−2.2344	0.4552	−2.2343	0.4553	−2.2343	0.4553	−2.2343	0.4553
k_f		1.0416		1.0416		1.0416		1.0416		1.0374

Model M1 has a lithosphere viscosity of 10^{21} Pa s which is the same as the mantle; thus, this is actually a two-layer model without lithosphere. The lithosphere of models M2–M5 have viscosities of 10^{24}, 10^{26}, 10^{29}, and ∞ Pa s, respectively.

The degree 2 potential tidal Love numbers of models M1–M5 are shown in Table 3, where the inverse relaxation time s_i has unit 1/ka. Following Sabadini et al. (2016), we can see that the two-layer model M1 only contains two relaxation modes, C_0 corresponding to the core-mantle boundary and M_0 corresponding to the surface. When a viscoelastic layer with the same density is added to the model (M2–M5), two additional transition modes, $\bar{T}_1$ and $\bar{T}_2$, are triggered if the Maxwell time on either side of the boundary is different. In the case of model M2, these two additional modes have relaxation times not too different from the dominant modes (C_0 and M_0 in this case). Consequently, the delayed relaxation of both $\bar{T}_1$ and $\bar{T}_2$ is not large enough to cause a remnant bulge. However, in the case of M3 and M4, as the viscosity of the lithosphere increases, the relaxation time for one of the $\bar{T}$ modes increases with the same order as the viscosity. It is this $\bar{T}$ mode that determines if the remnant bulge is present. As the viscosity of the lithosphere increases further and eventually approaches infinity, as is the case in model M5, the $\bar{T}_1$ mode disappears and its mode strength $-k_1/s_1$ becomes absent in the fluid Love number k_f. It can be seen that the difference in the fluid Love number between M5 and M4 is almost the same as the mode strength of $\bar{T}_1$ in M4: $k_f^{M4} - k_f^{M5} \approx (k_1/s_1)^{M4}$. The remnant bulge is dealt with in previous studies by either those dealing with an elastic lithosphere (Cambiotti et al., 2010; Chan et al., 2014; Harada, 2012; Mitrovica et al., 2005) or viscoelastic lithosphere (Cambiotti et al., 2010; Moore et al., 2017) by isolating this part of the Love number and formulating the influence of it separately.

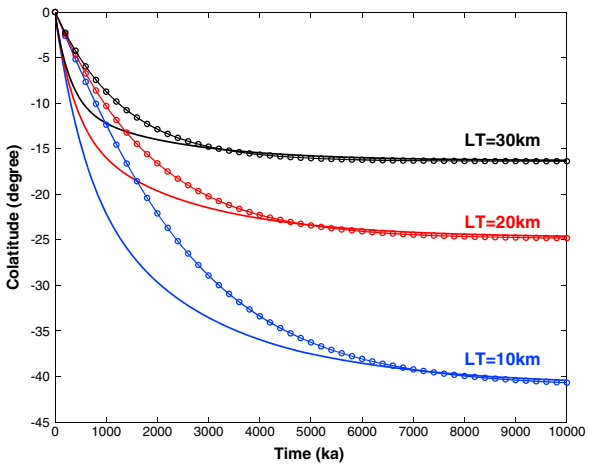

Figure 7. Polar wander in the *X-Z* plane for the Earth models with different lithosphere thickness triggered by a point mass of 2×10^{19} kg attached at the surface at 20° colatitude. Solid lines show results obtained with the full-Maxwell method from this paper, the line dots are calculated with the method by Chan et al. (2014) which is based on the quasi-fluid approximation.

One of the advantages of the full-Maxwell method is that we can choose any value for the initial loading time T_h. This enables us to simulate the influence of the remnant bulge without any extra formulation. To include such a bulge caused by a very slow relaxation mode, we only need to set the initial loading time T_h to a value large enough so that this slow mode is fully relaxed to the centrifugal force, according to the condition in equation (18). For instance, for the model M4 in Table 3, we can set $T_h = 1 \times 10^9$ ka which guarantees that the $\bar{T}_1$ mode is relaxed. In practice, we do not need to simulate the case with a fully elastic layer. Instead, we can always set the viscosity of the layer high enough to guarantee that its relaxation within the considered time can be ignored. In that case, the lithosphere is effectively elastic.

Now we demonstrate the effect of a remnant bulge with the full-Maxwell method and compare the results with those obtained by applying the quasi-fluid approximation. A more realistic SG6 model is used, in contrast with those shown in Figure 4 where the slowest mode is ignored. Three cases with different thickness of the lithosphere are considered and the viscosity of this layer is set to 10^{31} Pa s so that within the considered time span (10 Ma), the relaxation of the slowest mode can be ignored. We compare our results with those obtained by using the method of Chan et al. (2014) which is based on the quasi-fluid approximation. The results are shown in Figure 7. While predicting the same end position of TPW, the quasi-fluid approximation gives a much slower transient response.

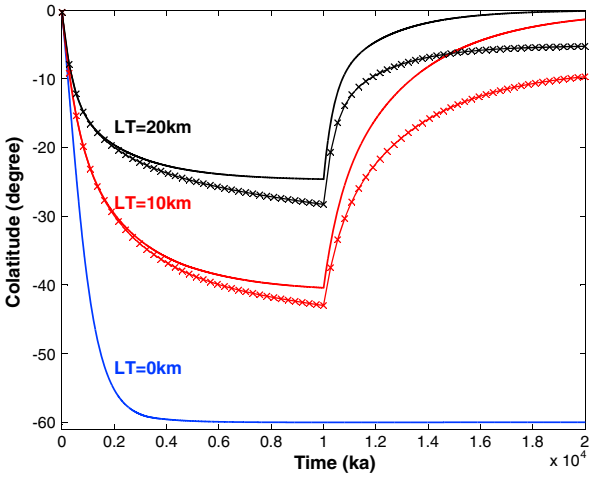

Figure 8. A point mass of 2×10^{19} kg attached at the surface at 30° colatitude and removed after 10 Ma. Lines are for models with lithosphere viscosity of 10^{31} Pa s and line crosses are for models with lithosphere viscosity of 10^{27} Pa s.

Next we show the effect of a viscoelastic lithosphere whose viscosity has a relaxation time which is comparable with the considered time span. This issue is important because whether or not the lithosphere can relax during the considered period can affect the TPW behavior both in the short term (e.g., the speed) and the long term. The comparison between the effect of an effectively elastic and a viscoelastic lithosphere on small-range TPW (less than 2°) has been done by Cambiotti et al. (2010) using a linear scheme. Here we show the effect when large-angle TPW is considered. For this issue Moore et al. (2017) extend the theory in Chan et al. (2014) and consider the slowest mode(s) separately while applying the quasi-fluid approximation to the rest of the modes. Apart from the bias introduced by the quasi-fluid approximation as shown in Figure 7, another problem of this approach is that for a complex multilayered model like the SG6 Earth model with its lithosphere viscosity smaller than a certain value (e.g., 10^{28} Pa s for SG6 model), the slowest mode might not be the $\bar{T}_1$ mode from the lithosphere but one of the M modes ($M2$, $M3$, …) which is generated by a density difference of the inner layers. Moreover, there might not be a large difference in the relaxation time between two modes (such as cases M3 and M4 in Table 3); as a result, it is not clear which modes need to be modeled separately. Our approach does not have this limitation. Similar to the case of an effectively elastic lithosphere, we only need to choose a large enough value for T_h. Here the SG6 model with lithospheric thicknesses of 0, 10, and 20 km and with viscosities of 10^{27} and 10^{31} Pa s is used. A mass anomaly of 2×10^{19} kg is placed at 30° colatitude for 10 Ma, then removed. Within the considered time span of 20 Ma, the lithosphere with viscosity of 10^{31} Pa s can be considered as effectively elastic while that with a viscosity of 10^{27} Pa s is partially relaxed. The result is shown in Figure 8. We see that the behavior of the TPW is very sensitive to the thickness of the lithosphere. A thicker lithosphere gives stronger resistance against TPW as well as a faster rebounding of the rotational axis when the triggering load is removed. Due to the partial relaxation of the $\bar{T}_1$ mode, which allows the equatorial bulge

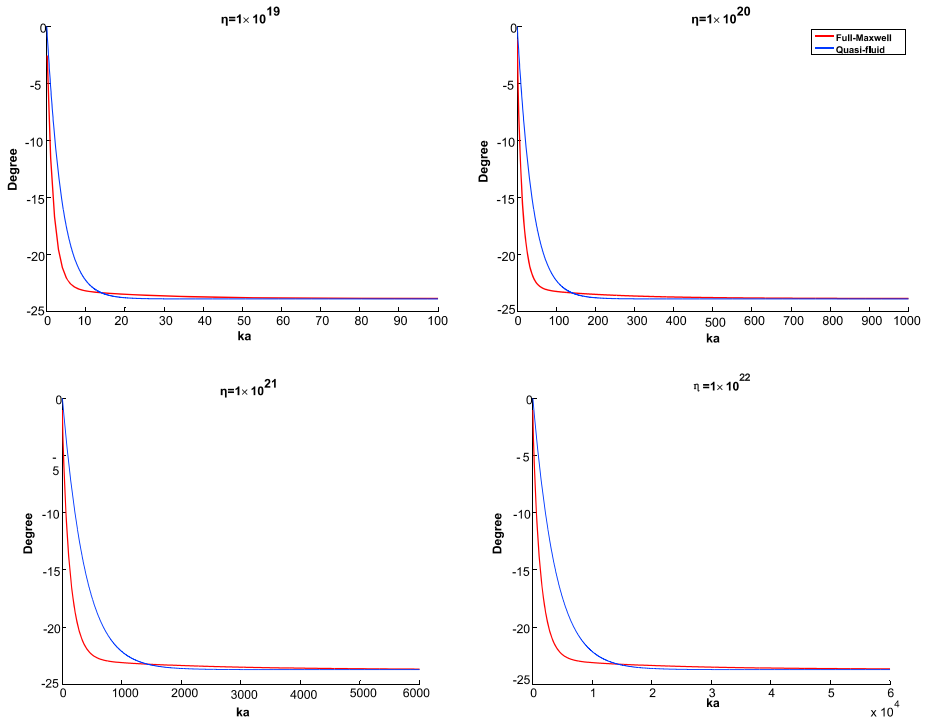

Figure 9. TPW on Mars triggered by a mass anomaly of 3.5×10^{19} kg which is attached at the surface at 45° latitude for four different values of mantle viscosity. This magnitude is about the same as for $Q = 1$ of the normalized load parameter Q defined in Willemann (1984).

to adjust faster for the high viscosity lithosphere, the TPW for models with a low viscosity lithosphere is larger and the rotational axis cannot go back to its original position after the mass anomaly is removed.

We also apply our method to a model of Mars to compare the speed of TPW on Mars calculated by the two methods. We establish a five-layer model whose density and rigidity approximates the model in Zharkov and Gudkova (2005) which contains a 50 km lithosphere. The viscosity of the model is divided into an effectively elastic lithosphere and a uniform mantle of viscosities 10^{19} Pa s, 10^{20} Pa s, 10^{21} Pa s, and 10^{22} Pa s which covers the value used in most recent studies (Breuer & Spohn, 2006; Hauck & Phillips, 2002). We load the model with a surface mass anomaly of magnitude 3.5×10^{19} kg (which is about the magnitude for $Q = 1$ for the normalized load parameter Q defined in Willemann (1984) and used by Chan et al. (2014) and Matsuyama and Nimmo (2007)) placed at 45° latitude. The results are shown in Figure 9. Similar to the Earth model, the quasi-fluid approximation has a large underestimation of the speed for most of the duration of the TPW. The instantaneous speed from the full-Maxwell method is, for all four viscosities, about 4.6 times as large as those obtained based on the quasi-fluid approximation. The reason for this is, as mentioned before, the underestimation of the equatorial bulge readjustment when the approximation is adopted. When the rotational axis approaches its end position, the speed of TPW obtained from the full-Maxwell method drops faster than for the quasi-fluid approximation which results in the end position being reached later. Generally, the method based on the quasi-fluid approximation underestimates the time it takes for a mass anomaly to reach its end position by about half, compared to the full-Maxwell method.

5. TPW on a Model Without Hydrostatic Equilibrium

In practice, a physical model (consisting of layers with given density, rigidity, and viscosity) can be derived from a geochemical model and the density profile matches the total mass and/or gravitational data. However, it can happen that the predicted tidal fluid Love number based on the physical model does not match the observed value for the present-day rotational speed Ω. By assuming that the model is in hydrostatic equilibrium, the fluid Love number can be estimated from the observed difference in the polar and equatorial moments of inertia $C - A$ (Mound et al., 2003):

$$k_f^{\text{obs}} = \frac{3G}{a^5\Omega^2}(C - A)_{\text{obs}} \tag{24}$$

For the Earth, this issue appears to have been studied first by Mitrovica et al. (2005) who introduced the β correction term to the tidal fluid Love number when the present-day TPW speed is estimated. Usually, it is considered that this extra nonhydrostatic contribution stems from mantle convection. Here we simulate another possible cause for this contribution and its effect on TPW. Before the TPW starts, the lithosphere is not in hydrostatic equilibrium, or more specifically, the permanent shape of the elastic lithosphere does not match the present-day rotational speed. The stress-free flattening of the elastic layer can be either larger or smaller because the rotational speed during the formation of the planet (or moon) was either faster or slower than the present-day value. We demonstrate here the influence on the TPW of a lithosphere with the same thickness but in different hydrostatic state.

Since the influence of each relaxation mode s_i is formulated separately in terms $a_{i,j,p,q}(t)$ and $c_{i,j,p,q}(t)$ in equations (A1a)–(A1c), we can set both the initial loading potential characterized by $\omega_i(t)$ and the loading period differently for each relaxation mode to simulate the model being in a different hydrostatic state. For each relaxation mode s_i, we set the initial loading period as T_{i_h} and the rotational speed as $\boldsymbol{\omega}_{i_0}$. In contrast to equations (16a)–(16c), we now have

$$T_{0,i} = 0 \tag{25a}$$

$$T_{1,i} = T_{i_h} \tag{25b}$$

$$\left(W_{1,0}, W_{2,0}, W_{3,0}\right)_i = \left(W_{1,1}, W_{2,1}, W_{3,1}\right)_i = \boldsymbol{\omega}_{i_0} \tag{25c}$$

In the following, we show that the choice of the hydrostatic state is as important as the choice of the model. We demonstrate this concept using SG6 models with a thin (10 km) and thick (20 km) lithosphere. As shown in Figure 8, when the models are in hydrostatic equilibrium, different lithospheric thicknesses result in significantly different TPW behavior. This SG6 model is put into two categories which results in four scenarios in total.

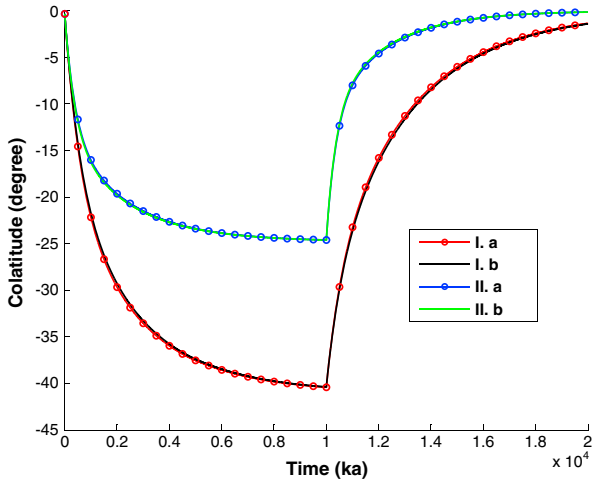

Figure 10. TPW for a point mass of 2×10^{19} kg attached at the surface at 30° colatitude and removed after 10 Ma. Red and blue lines are models with an effectively elastic (viscosity 10^{31} Pa s) lithosphere with thickness of 10 km and 20 km, respectively, which are in hydrostatic equilibrium. Green and black lines represent models with a lithosphere thickness of 10 km and 20 km, respectively, and their lithospheres initially contribute the same to the moment of inertia as the models in hydrostatic equilibrium.

Category I: Scenario Ia. A thin-lithosphere model in hydrostatic equilibrium with the present-day rotational speed.Ib. A thick-lithosphere model whose slowest mode has relaxed so that its mode strength is equal to that of the thin lithosphere model:

$$\left(\frac{k_1}{s_1}\right)^{\text{thick}} \times \left(1 - e^{s_1 T_{h_1}}\right) = \left(\frac{k_1}{s_1}\right)^{\text{thin}} \tag{26}$$

Since other modes are much faster than the slowest mode, this T_{h_1} is set for all the modes. In this way, all other modes except the slowest one are fully relaxed. The partial relaxation of the slowest mode of the thick-lithosphere model has the same strength as the slowest mode of the thin-lithosphere model.

Scenario Ib is created to simulate that the rotational speed during the formation of the lithosphere was slower than present-day.

Category II: Scenario IIa. A thick-lithosphere model in hydrostatic equilibrium with the present-day rotational speed.IIb. A thin-lithosphere model whose slowest mode has fully relaxed for a faster rotational speed of

$$\omega_{1_0}^{\text{Thin}} = \sqrt{\frac{\left(k_1/s_1\right)^{\text{Thick}}}{\left(k_1/s_1\right)^{\text{Thin}}}}\omega_0 \tag{27}$$

where ω_0 is the present-day rotational speed. $\left(k_1/s_1\right)^{\text{Thick}}$ and $\left(k_1/s_1\right)^{\text{Thin}}$ are the mode strengths of the slowest modes of the thick and thin lithosphere model, respectively.

Scenario IIb corresponds to the situation that the rotational speed during the formation of the lithosphere is faster than the present-day value. With equations (26) and (27), we configure the scenarios of models without hydrostatic equilibrium, Ib and IIb, such that the influence of the slowest mode has the same contribution to the inertia tensor of the entire model at the start of the simulation in each category. We test the model with an effectively elastic lithosphere (viscosity 10^{31} Pa s) with the same loading as those in Figure 8. The results are shown in Figure 10.

As we can see in Figure 10, although the models in each category have different thicknesses of the lithosphere and hydrostatic states, the performance of TPW is almost identical. This can be understood as follows: when the lithosphere is thin enough (e.g., less than 100 km for the Earth's case), the influence of changing the properties of this layer (thickness, rigidity, and viscosity) is very small on modes other than $\bar{T}_1$ and $\bar{T}_2$ generated from the nonlithosphere part of the model. Its largest effect is, as shown in Figure 4, a remnant bulge which resists the readjustment of the equatorial bulge. Once we choose a proper hydrostatic state so that the same contribution to the inertia tensor is guaranteed from the lithosphere of a different model, the path of TPW will also be almost the same. As for the issue concerning the difference between the observed and model predicted flattening, it can be seen from equation (27) that if the elastic layer generates a mode with strength $-k_1/s_1$ and the rotational speed during its formation is Ω_0, and Ω_c at present-day, then this elastic layer would cause an extra flattening represented in the observed fluid Love number as

$$\Delta k_f^{\text{obs}} = -\frac{k_1}{s_1}\left[\left(\frac{\Omega_0}{\Omega_c}\right)^2 - 1\right] \tag{28}$$

For the Earth model, for instance, considering that 6 Ma ago the rotational speed of Earth was about 15% faster (Zahnle & Walker, 1987), the rotational speed during the formation of the lithosphere would be even higher considering that tidal dissipation started when the Earth-Moon system formed about 4.5 Ga ago. An elastic lithosphere of 80 km with a rotational speed during formation that is 30% faster than the present-day speed would cause the observed fluid Love number to increase by about 0.01.

We conclude that for the study of TPW for a model with a lithosphere, it is necessary to know both the initial stress-free shape of the lithosphere as well as its thickness before a correct TPW behavior can be predicted.

This can be significant for the study of TPW on Mars since it has less tectonic activity compared to Earth to release the stress in its lithosphere, which results in a higher chance that the Mars is not in hydrostatic equilibrium.

6. Conclusion

We have established a new semianalytical method for calculating large-angle true polar wander (TPW) which is consistent with the complete scheme of Maxwell rheology, meaning that both fast and slow modes are correctly taken into account, in contrast with previous studies which adopt the quasi-fluid approximation that approximate the Love number. We extend the scheme of the linearized Liouville equation in Hu et al. (2017) which can also be used to simulate the mega-wobble on Venus. The influence of the delayed relaxation of elastic or highly viscous layers as well as models in different hydrostatic states (e.g., not in hydrostatic equilibrium) has been studied. With the help of our model, the following conclusions can be drawn:

1. The quasi-fluid approximation can introduce a large error in the transient response for a time-dependent solution. The TPW speed on Earth and Mars based on the quasi-fluid approximation can be underestimated, while the speed of the rotational axis approaching the end position on Venus is overestimated.
2. Depending on the considered period, the TPW for a model with a viscoelastic lithosphere can have a larger displacement and a weaker restoring response compared to a model with an (effectively) elastic lithosphere. Due to the sensitivity of TPW to the shape of the lithosphere, the viscosity of the lithosphere needs to be taken into account when the studied period is not much shorter than the relaxation time of the lithosphere.
3. The permanent shape of the elastic lithosphere can have a large effect on the TPW and this can be an additional explanation for the difference between the observed and model-predicted flattening of a rotating body.

Thus, studies involving TPW can benefit from our method to achieve better accuracy in the pole path, especially while taking into account a viscous lithosphere or nonhydrostatic background. Our method can also be extended to tidally deformed models. In this paper we applied algorithm 2 of Hu et al. (2017) to calculate the rotational perturbation. In the same paper, a new iterative procedure was also presented to combine both the rotational and tidal perturbation (algorithm 3). Combining this algorithm with the analytical solution for the change in the moment of inertia presented in the present paper can give a semianalytical solution for large-angle reorientations of rotating tidally deformed bodies.

Appendix A: Expressions for $A_{i,j}(t)$, $B_{i,j}(t)$, $C_{i,j}(t)$, and $D_{i,j}(t)$

$$k^T(t) * \omega_i(t)\omega_j(t)|_{t=T_n} = A_{i,j}\left(T_n\right) + B_{i,j} \tag{A1a}$$

$$\frac{\mathrm{d}\left[k^T(t) * \omega_i(t)\omega_j(t)\right]}{\mathrm{d}t}|_{t=T_n} = C_{i,j}\left(T_n\right) + D_{i,j} \tag{A1b}$$

where

$$A_{i,j}(t) = \sum_{p=1}^{n}\sum_{q=1}^{m} a_{i,j,p,q}(t) \tag{A2}$$

$$C_{i,j}(t) = \sum_{p=1}^{n}\sum_{q=1}^{m} c_{i,j,p,q}(t) \tag{A3}$$

and

$$B_{i,j} = k_e^T W_{i,n} W_{j,n} \tag{A4a}$$

$$D_{i,j} = \frac{k_e^T\left(W_{i,n-1}W_{j,n} + W_{i,n}\left(W_{j,n-1} - 2W_{j,n}\right)\right)}{T_{n-1} - T_n} \tag{A4b}$$

where for $t > T_p$

$$a_{i,j,p,q}(t) = \frac{k_q}{(T_{p-1}-T_p)^2 s_q^3}\Big(e^{s_q(t-T_{p-1})}\left(W_{i,n}\left(W_{j,n-1}\left(\left(T_p-T_{p-1}\right)s_q-2\right)+2W_{j,n}\right)\right.$$
$$+W_{i,n-1}\left(W_{j,n-1}\left(\left(T_{p-1}-T_p\right)s_q\left(\left(T_{p-1}-T_p\right)s_q+2\right)+2\right)+W_{j,n}\left(\left(T_p-T_{p-1}\right)s_q-2\right)\right)\right) \quad \text{(A5)}$$
$$-e^{s_q(t-T_p)}\left(W_{i,n-1}\left(W_{j,n}\left(\left(T_{p-1}-T_p\right)s_q-2\right)+2W_{j,n-1}\right)\right.$$
$$\left.+W_{i,n}\left(\left(\left(T_{p-1}-T_p\right)s_q-2\right)\left(\left(T_{p-1}-T_p\right)s_qW_{j,n}+W_{j,n-1}\right)+2W_{j,n}\right)\right)\Big)$$

$$c_{i,j,p,q}(t) = \frac{k_q e^{-s_qT_{p-1}}}{(T_{p-1}-T_p)^2 s_q^2}\Big(e^{ts_q}\left(W_{i,n}\left(W_{j,n-1}\left(\left(T_p-T_{p-1}\right)s_q-2\right)+2W_{j,n}\right)\right.$$
$$+W_{i,n-1}\left(W_{j,n-1}\left(\left(T_{p-1}-T_p\right)s_q\left(\left(T_{p-1}-T_p\right)s_q+2\right)+2\right)+W_{j,n}\left(\left(T_p-T_{p-1}\right)s_q-2\right)\right)\right) \quad \text{(A6)}$$
$$-e^{s_q(T_{p-1}-T_p+t)}\left(W_{i,n-1}\left(W_{j,n}\left(\left(T_{p-1}-T_p\right)s_q-2\right)+2W_{j,n-1}\right)\right.$$
$$\left.+W_{i,n}\left(\left(\left(T_{p-1}-T_p\right)s_q-2\right)\left(\left(T_{p-1}-T_p\right)s_qW_{j,n}+W_{j,n-1}\right)+2W_{j,n}\right)\right)\Big)$$

and for $t \le T_p$

$$a_{i,j,p,q}(t) = \frac{k_q}{(T_{p-1}-T_p)^2 s_q^3}\Big(W_{i,n}\left(W_{j,n-1}\left(s_q\left(s_q\left(t-T_{p-1}\right)\left(t-T_p\right)+\left(T_p-T_{p-1}\right)e^{s_q(t-T_{p-1})}\right.\right.\right.$$
$$\left.-T_{p-1}-T_p+2t\right)-2e^{s_q(t-T_{p-1})}+2\Big)$$
$$\left.+W_{j,n}\left(2\left(e^{s_q(t-T_{p-1})}-1\right)-s_q\left(t-T_{p-1}\right)\left(s_q\left(t-T_{p-1}\right)+2\right)\right)\right) \quad \text{(A7)}$$
$$+W_{i,n-1}\left(W_{j,n-1}\left(2\left(e^{s_q(t-T_{p-1})}-1\right)+s_q\left(\left(T_{p-1}-T_p\right)\left(\left(T_{p-1}-T_p\right)s_q+2\right)e^{s_q(t-T_{p-1})}\right.\right.\right.$$
$$\left.+\left(t-T_p\right)\left(s_q\left(T_p-t\right)-2\right)\right)\right)$$
$$\left.+W_{j,n}\left(s_q\left(s_q\left(t-T_{p-1}\right)\left(t-T_p\right)-T_{p-1}-T_p+2t\right)+\left(\left(T_p-T_{p-1}\right)s_q-2\right)e^{s_q(t-T_{p-1})}\right)+2W_{j,n}\right)\Big)$$

$$c_{i,j,p,q}(t) = \frac{k_q e^{-s_qT_{p-1}}}{(T_{p-1}-T_p)^2 s_q^2}\Big(e^{ts_q}\left(W_{i,n}\left(W_{j,n-1}\left(\left(T_p-T_{p-1}\right)s_q-2\right)+2W_{j,n}\right)\right.$$
$$+W_{i,n-1}\left(W_{j,n-1}\left(\left(T_{p-1}-T_p\right)s_q\left(\left(T_{p-1}-T_p\right)s_q+2\right)+2\right)+W_{j,n}\left(\left(T_p-T_{p-1}\right)s_q-2\right)\right)\right) \quad \text{(A8)}$$
$$-e^{T_{p-1}s_q}\left(W_{i,n}\left(W_{j,n-1}\left(s_q\left(T_{p-1}+T_p-2t\right)-2\right)+2W_{j,n}\left(s_q\left(t-T_{p-1}\right)+1\right)\right)\right.$$
$$\left.+W_{i,n-1}\left(2W_{j,n-1}\left(s_q\left(t-T_p\right)+1\right)+W_{j,n}\left(s_q\left(T_{p-1}+T_p-2t\right)-2\right)\right)\right)\Big)$$

Appendix B: Iterative Algorithm for Calculating TPW

1. Assume that step i starts at time t_i with the vector of the rotation being $\boldsymbol{\omega}^i = \Omega^i(\omega_1^i, \omega_2^i, \omega_3^i)$ and ends at time t_{i+1} with the vector of the rotation being $\boldsymbol{\omega}^{i+1}$. For the first iteration we assume that the vector of the rotation does not change: $\boldsymbol{\omega}^{i+1} = \boldsymbol{\omega}^i$.
2. Obtain $\Delta\mathbf{I}$ and its derivative $\Delta\dot{\mathbf{I}}$ from equations (12a) and (12b). With $\mathbf{Q}$ as defined in equation (15) being the coordinate transformation matrix from the body-fixed coordinates to the local coordinates where the Z axis aligns with the direction of the rotation, the inertia tensors in the transformed coordinates are obtained by $\Delta\mathbf{I}_1 = \mathbf{Q}^T\Delta\mathbf{I}\mathbf{Q}$ and $\Delta\dot{\mathbf{I}}_1 = \mathbf{Q}^T\Delta\dot{\mathbf{I}}\mathbf{Q}$.
3. Substitute $\Delta\mathbf{I}_1$ and $\Delta\dot{\mathbf{I}}_1$ into equations (14a)–(14c) and obtain $\boldsymbol{\omega}' = \Omega^i(m_1, m_2, 1+m_3)^T$. Normalize this vector as $\boldsymbol{\omega}' = \Omega^{i+1}\bar{\boldsymbol{\omega}}'$, where $\bar{\boldsymbol{\omega}}'$ is the direction of the perturbed rotational axis in the local coordinate system and transform back into the body-fixed frame to obtain $\boldsymbol{\omega}^{i+1} = \Omega^{i+1}\mathbf{Q}\,\bar{\boldsymbol{\omega}}'$.
4. Substitute $\boldsymbol{\omega}^{i+1}$ into step 2 until the result converges.

Appendix C: Governing Equation for the Case $B < C < A$ and $B > C > A$

For the case $B > C > A$, we assume that the changes in the inertia tensor are linear:

$$\Delta I_{13}(t) = a_1 + b_1 t \quad \text{(C1a)}$$

$$\Delta I_{23}(t) = a_2 + b_2 t \quad \text{(C1b)}$$

Then equations (20a)–(20c) can be solved analytically which results in

$$m'_1(t) = \sqrt{\frac{B}{A(C-A)^3(B-C)\Omega^2}}\sinh\left(\sqrt{\frac{(C-A)(B-C)}{AB}}\Omega\Delta t\right)\left((C-A)\Delta I_{23}(t) - C\Delta\dot{I}_{13}(t)\right) - \cosh\left(\sqrt{\frac{(C-A)(B-C)}{AB}}\Omega\Delta t\right)\left(\frac{\Delta I_{13}(t)}{C-A} + \frac{C\Delta\dot{I}_{23}(t)}{\Omega(C-A)(B-C)}\right) + \left(\frac{\Delta I_{13}(t)}{C-A} + \frac{C\Delta\dot{I}_{23}(t)}{\Omega(C-A)(B-C)}\right) \tag{C2}$$

$$m'_2(t) = \sqrt{\frac{A}{B(C-A)(B-C)^3\Omega^2}}\sinh\left(\sqrt{\frac{(C-A)(B-C)}{AB}}\Omega\Delta t\right)\left((C-B)\Delta I_{13}(t) + C\Delta\dot{I}_{23}(t)\right) + \cosh\left(\sqrt{\frac{(C-A)(B-C)}{AB}}\Omega\Delta t\right)\left(\frac{\Delta I_{23}(t)}{B-C} - \frac{C\Delta\dot{I}_{13}(t)}{\Omega(C-A)(B-C)}\right) - \left(\frac{\Delta I_{23}(t)}{B-C} - \frac{C\Delta\dot{I}_{13}(t)}{\Omega(C-A)(B-C)}\right) \tag{C3}$$

where $\sinh(u)$ and $\cosh(u)$ are hyperbolic functions

$$\sinh(u) = \frac{e^u - e^{-u}}{2} \tag{C4a}$$

$$\cosh(u) = \frac{e^u + e^{-u}}{2} \tag{C4b}$$

When Δt is small enough, we can apply approximation $\sinh(\theta) \approx \theta$ and $\cosh(\theta) \approx 1 - \theta^2/2$. Ignoring the derivative terms of the inertia tensor simplifies equations (C2) and (C3) into

$$m'_1(t) = \frac{(B-C)\Omega^2\Delta I_{13}(t)\Delta t^2 + 2B\Omega\Delta I_{23}(t)\Delta t}{2AB} \tag{C5a}$$

$$m'_2(t) = \frac{-(C-A)\Omega^2\Delta I_{23}(t)\Delta t^2 - 2A\Omega\Delta I_{13}(t)\Delta t}{2AB} \tag{C5b}$$

The same procedure can be applied to the case $A > C > B$, which results in

$$m''_1(t) = \frac{(C-B)\Omega^2\Delta I_{13}(t)\Delta t^2 + 2B\Omega\Delta I_{23}(t)\Delta t}{2AB} \tag{C6a}$$

$$m''_2(t) = \frac{-(A-C)\Omega^2\Delta I_{23}(t)\Delta t^2 - 2A\Omega\Delta I_{13}(t)\Delta t}{2AB} \tag{C6b}$$

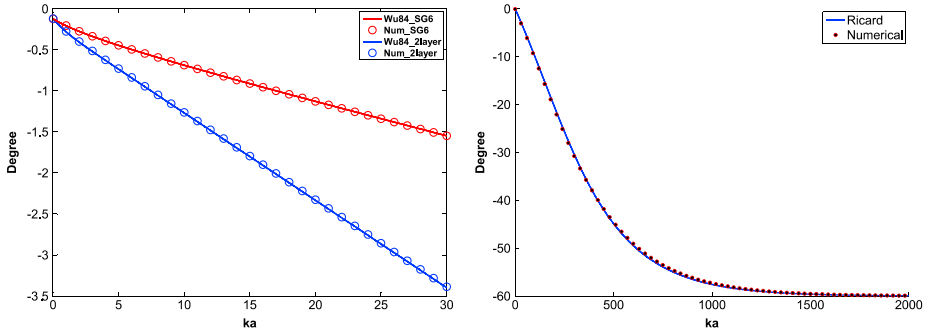

Figure D1. (left) The polar wander path in the *x*-*z* plane of the two-layer (blue) and SG6 (red) Earth models triggered by a mass anomaly of 2×10^{19} kg attached at 45° colatitude in the *x*-*z* plane. Lines show the results with the semianalytical method of Wu and Peltier (1984) (Figure D1, left). Circles represent our method. (right) The polar wander path in the *x*-*z* plane of the two-layer Earth model triggered by a mass anomaly of 2×10^{19} kg attached at 30° colatitude in the *x*-*z* plane. Lines show the results with the semianalytical method of Ricard et al. (1993) (Figure D1, left). Circles represent our methods.

Appendix D: Validation of the Iterative Algorithm

Figure D1 contains the validation done in Hu et al. (2017). The iterative procedure shown in Appendix B has been compared for short-term small-angle TPW, where linear method (Wu & Peltier, 1984) is accurate. For large-angle TPW we compare results against the nonlinear method from Ricard et al. (1993). That method can only simulate TPW for models without large relaxation time contrast in the modes (Hu et al., 2017). It can be seen that our iterative procedure matches the results obtained with the methods from Wu and Peltier (1984) and Ricard et al. (1993) very well.

Acknowledgments
We thank two anonymous reviewers for their review and constructive suggestions. This research has been financially supported by the GO program of the Netherlands Organization for Scientific Research (NWO), project ALW-GO-12/11. All data used to produce the figures and the codes for the algorithm have been uploaded to *4TU Center for Research Data* (https://data.4tu.nl/) under the name of this paper.

References

Armann, M., & Tackley, P. J. (2012). Simulating the thermochemical magmatic and tectonic evolution of Venus's mantle and lithosphere: Two-dimensional models. *Journal of Geophysical Research*, *117*, E12003. https://doi.org/10.1029/2012JE004231

Bouley, S., Baratoux, D., Matsuyama, I., Forget, F., Séjourné, A., Turbet, M., & Costard, F. (2016). Late Tharsis formation and implications for early Mars. *Nature*, *531*(7594), 344–347.

Breuer, D., & Spohn, T. (2006). Viscosity of the Martian mantle and its initial temperature: Constraints from crust formation history and the evolution of the magnetic field. *Planetary and Space Science*, *54*(2), 153–169.

Cambiotti, G., Ricard, Y., & Sabadini, R. (2010). Ice age true polar wander in a compressible and non-hydrostatic Earth. *Geophysical Journal International*, *183*(3), 1248–1264. https://doi.org/10.1111/j.1365-246X.2010. 04791.x

Cambiotti, G., Ricard, Y., & Sabadini, R. (2011). New insights into mantle convection true polar wander and rotational bulge readjustment. *Earth and Planetary Science Letters*, *310*(3), 538–543.

Chan, N.-H., Mitrovica, J. X., Daradich, A., Creveling, J. R., Matsuyama, I., & Stanley, S. (2014). Time-dependent rotational stability of dynamic planets with elastic lithospheres. *Journal of Geophysical Research: Planets*, *119*, 169–188. https://doi.org/10.1002/2013JE004466

Farrell, W. E. (1972). Deformation of the Earth by surface loads. *Reviews of Geophysics*, *10*(3), 761–797.

Harada, Y. (2012). Long-term polar motion on a quasi-fluid planetary body with an elastic lithosphere: Semi-analytic solutions of the time-dependent equation. *Icarus*, *220*(2), 449–465.

Harada, Y., & Xiao, L. (2015). A timescale of true polar wander of a quasi-fluid Earth: An effect of a low-viscosity layer inside a mantle. *Physics of the Earth and Planetary Interiors*, *240*, 25–33.

Hauck, S. A., & Phillips, R. J. (2002). Thermal and crustal evolution of Mars. *Journal of Geophysical Research*, *107*(E7), 6–1–6-19. https://doi.org/10.1029/2001JE001801

Hu, H., van der Wal, W., & Vermeersen, L. L. A. (2017). A numerical method for reorientation of rotating tidally deformed viscoelastic bodies. *Journal of Geophysical Research: Planets*, *122*, 228–248. https://doi.org/10.1002/2016JE005114

Keane, J. T., Matsuyama, I., Kamata, S., & Steckloff, J. K. (2016). Reorientation and faulting of Pluto due to volatile loading within Sputnik Planitia. *Nature*, *540*(7631), 90–93.

Lambeck, K. (2005). *The Earth's variable rotation: Geophysical causes and consequences, Cambridge Monographs on Mechanics*. Cambridge, UK: Cambridge University Press.

Matsuyama, I., & Nimmo, F. (2007). Rotational stability of tidally deformed planetary bodies. *Journal of Geophysical Research*, *112*, E11003. https://doi.org/10.1029/2007JE002942

Mitrovica, J. X., Wahr, J., Matsuyama, I., & Paulson, A. (2005). The rotational stability of an ice-age Earth. *Geophysical Journal International*, *161*, 491–506.

Moore, K., Chan, N.-H., Daradich, A., & Mitrovica, J. (2017). Time-dependent rotational stability of dynamic planets with viscoelastic lithospheres. *Icarus*, *289*, 34–41.

Mound, J. E., Mitrovica, J. X., & Forte, A. M. (2003). The equilibrium form of a rotating Earth with an elastic shell. *Geophysical Journal International*, *152*(1), 237–241.

Nakada, M. (2007). True polar wander associated with continental drift on a hypothetical Earth. *Earth, Planets and Space*, *59*(6), 513–522.

Peltier, W. R. (1974). The impulse response of a Maxwell Earth. *Reviews of Geophysics*, *12*(4), 649–669.

Ricard, Y., Spada, G., & Sabadini, R. (1993). Polar wandering of a dynamic Earth. *Geophysical Journal International*, *113*(2), 284–298.

Sabadini, R., & Peltier, W. R. (1981). Pleistocene deglaciation and the Earth's rotation: Implications for mantle viscosity. *Geophysical Journal of the Royal Astronomical Society*, *66*(3), 553–578.

Sabadini, R., Yuen, D. A., & Boschi, E. (1982). Polar wandering and the forced responses of a rotating, multilayered, viscoelastic planet. *Journal of Geophysical Research*, *87*(B4), 2885–2903.

Sabadini, R., Vermeersen, B., & Cambiotti, G. (2016). *Global dynamics of the Earth: Applications of viscoelastic relaxation theory to solid-Earth and planetary geophysics* (2nd ed.). Netherlands: Springer.

Spada, G., Ricard, Y., & Sabadini, R. (1992). Excitation of true polar wander by subduction. *Nature*, *360*(6403), 452–454.

Spada, G., Sabadini, R., & Boschi, E. (1996). Long-term rotation and mantle dynamics of the Earth, Mars, and Venus. *Journal of Geophysical Research*, *101*(E1), 2253–2266.

Willemann, R. J. (1984). Reorientation of planets with elastic lithospheres. *Icarus*, *60*, 701–709.

Wu, P., & Peltier, W. R. (1984). Pleistocene deglaciation and the Earth's rotation: A new analysis. *Geophysical Journal of the Royal Astronomical Society*, *76*(3), 753–791.

Zahnle, K., & Walker, J. C. (1987). A constant daylength during the Precambrian era? *Precambrian Research*, *37*(2), 95–105.

Zharkov, V. N., & Gudkova, T. V. (2005). Construction of Martian interior model. *Solar System Research*, *39*(5), 343–373. https://doi.org/10.1007/s11208-005-0049-7